

L'effet radiatif des poussières revisité

Sommaire

3.1 Préface	39
3.2 Abstract	43
3.3 Introduction	43
3.4 Modeling approach	44
3.4.1 “Ockert-Bell et al.” model (case 1 simulation)	45
3.4.2 “Wolff et al.” model (case 2 simulation)	47
3.4.3 TES-normalized interactive dust model (case 3 simulation)	49
3.5 Results using a prescribed dust vertical distribution	51
3.5.1 “Ockert-Bell et al.” model	52
3.5.2 Effect of the new “Wolff et al.” radiative properties	52
3.6 Results of the semi-interactive dust model	56
3.6.1 Role of the dust depth and particle size	56
3.6.2 Remaining temperature biases	58
3.7 Conclusion	58

3.1 Préface

Les poussières atmosphériques contrôlent en premier lieu la température de Mars, et la modélisation précise de leur répartition, ainsi que de leurs propriétés radiatives, est essentielle dans la construction d'un modèle climatique de la planète.

Le cycle des poussières de Mars présente des propriétés récurrentes d'une année sur l'autre, tout comme une impressionnante variabilité interannuelle. L'évolution latitudinale de l'opacité de poussière à $9.3 \mu\text{m}$ mesurée par TES est représentée sur la figure 3.1. Un phénomène récurrent est par exemple la forte opacité en poussière à l'approche du périhélie ($L_s = 251^\circ$), où plusieurs tempêtes de poussière locales se déclenchent chaque année. Cependant, le déclenchement de tempêtes globales, comme celle survenue l'année 25 à partir de $L_s = 180^\circ$, varie d'une année sur l'autre, et le cycle des poussières martien présente donc une forte variabilité interannuelle, extrêmement difficile à prévoir, notamment car elle dépend de mécanismes de soulèvement complexes.



Soulèvement matinal de poussière près du site de Viking 1 ($22.5^\circ\text{N}-48^\circ\text{W}$). La surface semble s'assombrir par retrait de la couche de poussière. Images MOC 23501 (rouge) et 23502 (bleu).

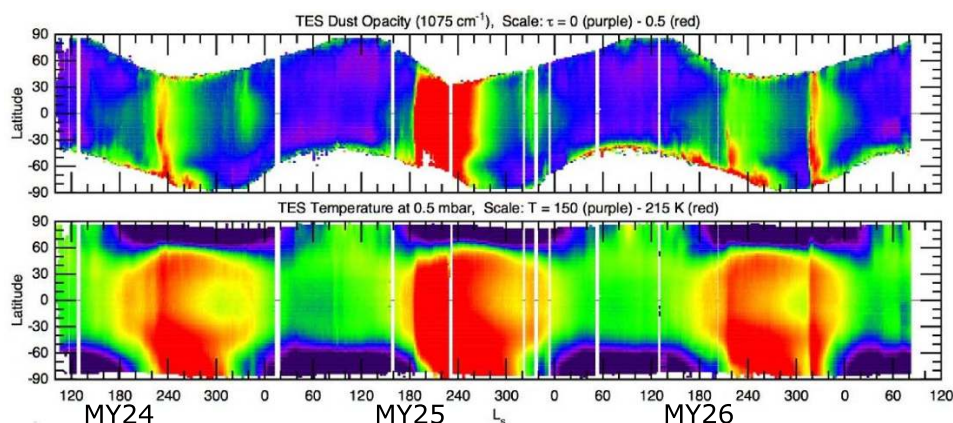


FIG. 3.1 – Opacité à $9.3 \mu\text{m}$ (1075 cm^{-1}) de la colonne de poussière observée par TES (haut) et température mesurée à 0.5 hPa (bas). L'opacité de poussière est donnée à une pression de référence de 6.1 hPa. L'échelle va de 0 (violet) à 0.5 (rouge) pour l'opacité de poussière, et de 150 à 215 K pour la température à 0.5 hPa. Les mesures couvrent une période allant de la fin de l'année martienne 24 à l'année 26. La tempête de poussière globale de l'année 25 (correspondant à l'année terrestre 2001) apparaît en rouge dès $L_s = 180^\circ$ dans le champ d'opacité (en haut), ce qui se traduit par une forte modification du champ de température (en bas). Figure adaptée de [Smith \(2006\)](#).

L'effet radiatif des poussières varie selon l'opacité de la couche et la taille des poussières. Pour mieux comprendre cet effet, une simulation 1D d'une atmosphère ensoleillée est présentée sur la figure 3.2. Elle montre les taux de chauffage solaire (« short-wave », traits pleins) et infrarouge (« longwave », pointillés) pour différentes opacités visibles de la couche de poussière (0.5, 1, 2 et 5). À plus de 1 km de la surface, les taux de chauffage solaire dominant nettement les taux de chauffage infrarouge, et sont de l'ordre de 30 K par jour pour une opacité visible courante de 0.5. Lorsque l'opacité augmente, les flux incidents en surface aux longueurs d'onde solaire diminuent (à droite de la figure), montrant l'extinction du rayonnement solaire par la couche de poussière. Le flux infrarouge reçu par la surface, au contraire, augmente avec l'opacité de la couche de poussière, cette dernière absorbant, et émettant donc davantage. En surface, le refroidissement de la surface due à la perte de flux solaire n'est pas compensée par le chauffage dû à l'augmentation du flux infrarouge, et la température de surface diminue, passant de 289 K à 258 K (voir les températures exactes en dessous de la figure 3.2). Lorsque l'opacité devient très élevée (courbes rouges), le taux de chauffage solaire dans les basses couches tend vers une valeur limite, par extinction du flux solaire par les couches supérieures.

Le comportement thermique de la couche de poussière dépend de ses propriétés radiatives, reflétées par les paramètres de diffusion simple. Ceux-ci sont présentés sur la figure 3.3, où il sont calculés pour différentes tailles des particules sphériques (code de Mie) à partir de l'indice de réfraction de la poussière déterminé par [Wolff et al. \(2006, 2009\)](#)* L'albédo de diffusion simple est très élevé là où l'énergie solaire reçue est maximale (voir la luminance de corps noir en pointillés sur la figure 3.3). Les températures sont donc extrêmement sensibles à la « clarté » de la poussière. La figure 3.3 montre enfin

Ce jeu de données sera décrit dans la partie 3.4.2.

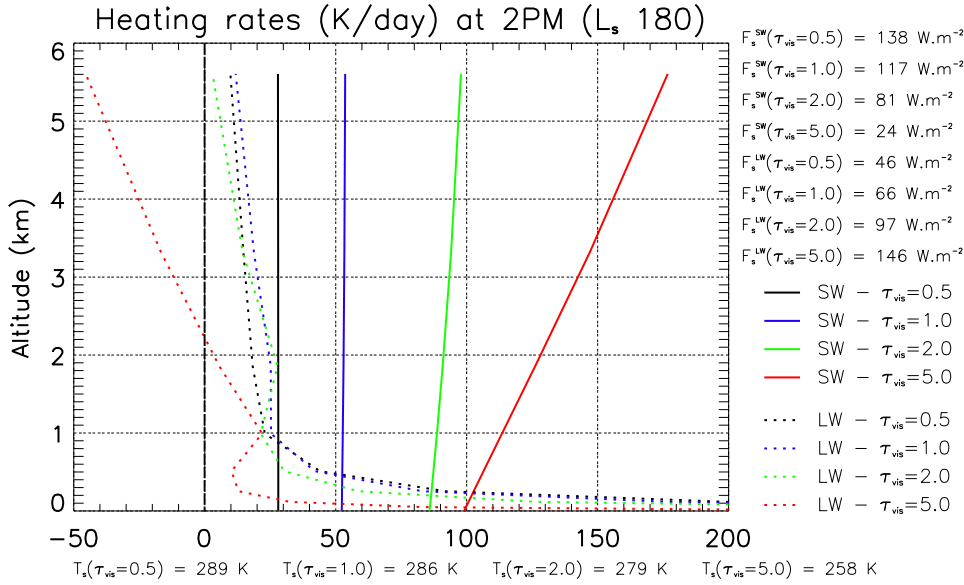


FIG. 3.2 – Taux de chauffage dans le domaine solaire (« shortwave », traits pleins) et infrarouge (« longwave », pointillés) pour différentes valeurs de l’opacité à $0.67 \mu m$ de la poussière. Les flux solaire et infrarouge incidents à la surface sont donnés à droite de la figure, et les températures de surface en dessous. Simulation 1D, réalisée à l’équateur, pour $L_s = 180^\circ$, à deux heures de l’après-midi.

la grande dépendance des propriétés radiatives à la taille des particules.

Les taux de chauffage par la poussière sont donc significatifs, et pour simuler fidèlement le climat de Mars, le modèle doit être guidé par l’opacité de poussière observée, par construction d’un scénario de poussière. L’opacité est donnée à une pression de référence de 6.1 hPa^* . Cela peut se justifier par intégration de l’équation 2.37, si le facteur devant dp est supposé constant, ce qui n’est vrai que si la couche de poussière est bien mélangée, et si les propriétés radiatives et la taille des particules sont supposées constantes. Cette approximation est bonne pour ajuster à un niveau de pression de référence l’opacité totale observée par TES, celle-ci variant souvent en fonction de la pression de surface et de l’inverse du cosinus de l’angle d’émergence, ce qui est le comportement attendu d’une couche de poussière bien mélangée (voir la page 203 de Smith, 2008).

Autrement dit la profondeur optique totale observée est multipliée par un facteur $610/p_s$, où p_s est la pression locale en surface.

Le modèle, une fois guidé par cette opacité de poussière, doit être en théorie capable de reproduire assez fidèlement les températures observées. Cependant, il a été difficile dans le passé d’obtenir des températures réalistes sans ajuster artificiellement cette opacité de guidage. Ce problème est abordé dans une première partie (3.5). Pour cela, les propriétés radiatives des poussières sont mises à jour, et le modèle est à nouveau évalué sans ajustement de l’opacité de poussière. Les résultats sont comparés aux observations, ainsi qu’aux résultats de la précédente version du modèle, qui utilisait des propriétés radiatives plus anciennes. Dans un deuxième temps, nous utilisons le modèle présenté au chapitre 2 pour améliorer la représentation de l’effet radiatif de la poussière. Un schéma de transport de la poussière est ajouté, et les propriétés radiatives, qui évo-

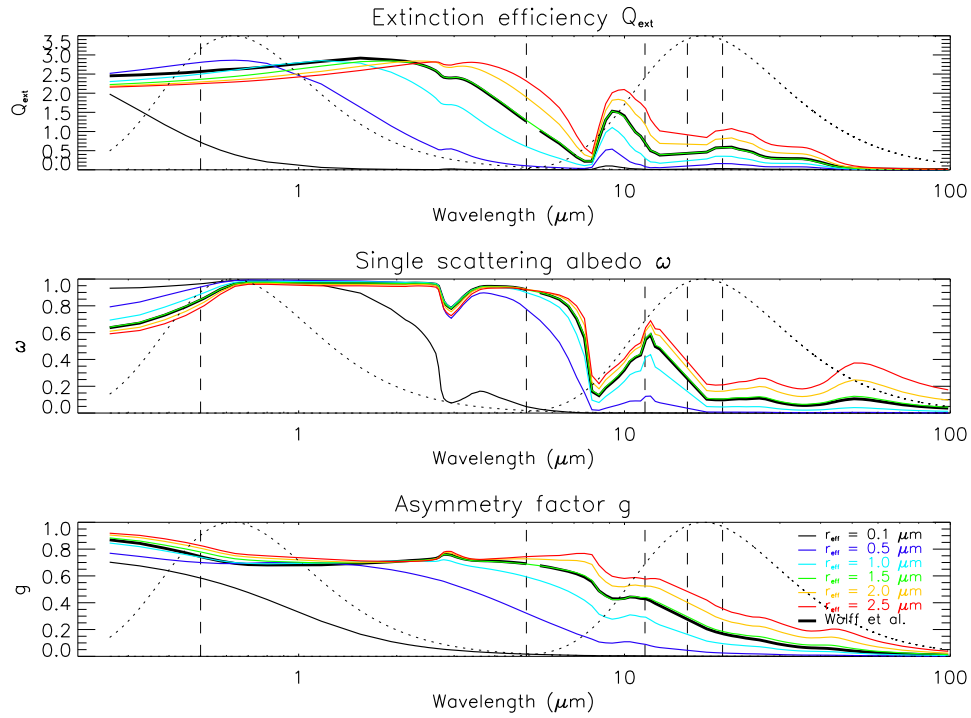


FIG. 3.3 – Les paramètres de diffusion simple de la poussière sont calculés pour différentes tailles de particules (r_{eff} de 0.1, 0.5, 1, 1.5, 2 et 2.5 μm) et une variance effective de 0.3 (distribution Gamma), en supposant des particules sphériques (code de Mie). Les propriétés radiatives de référence mesurés par Wolff et al. (2006, 2009) sont tracées en noir (distribution Gamma, code de T-Matrix, cylindres de rapport D/L de 1, r_{eff} de 1.5 μm et variance effective de 0.3). Comparer les courbes vertes et noires permet d'apprécier la différence entre les paramètres de diffusion simple de particules sphériques et de cylindres (voir notamment le facteur d'efficacité Q_{ext} aux longueurs d'onde visibles). Les luminances de corps noir à 5870 K et 210 K sont représentées en pointillé noir (l'aire est préservée, et $\lambda B_{\lambda}(T)$ est représentée).

luent dans le temps, sont calculées en utilisant les vrais profils de poussière simulés ainsi que la taille prévue des poussières*. Un taux de soulèvement homogène est utilisé sur l'ensemble de la planète, et le rayon effectif ainsi que la variance effective de la distribution de poussières soulevée sont ajustés afin que les tailles des poussières dans les premières couches de l'atmosphère soient compatibles avec celles observées par les rovers Spirit et Opportunity*. Les températures sont de nouveau analysées et comparées aux observations, et la validité de cette méthode est évaluée. Les différences de températures restantes sont commentées, et sont essentiellement dues à l'effet radiatif des nuages, qui sera abordé dans le chapitre 5.

Les variations de propriétés sont illustrées par la figure 3.3.

Voir la partie 3.4.3 pour plus de détails.

Ce chapitre est soumis pour publication, avec pour titre *Revisiting the radiative impact of dust on Mars using the LMD Global Climate Model* (J.-B. Madeleine, F. Forget, E. Millour, L. Montabone et M. J. Wolff).

3.2 Abstract

Airborne dust is the main driver of the Martian atmospheric temperature, and accurately accounting for its radiative effect in Global Climate Models (GCM) is essential. This implies the right modeling of the dust distribution and radiative properties, and when trying to simulate the true climate variability, the use of the observed dust column opacity to guide the model. A recurrent problem has been the inability of Mars GCMs to predict realistic temperatures while using both the observed dust radiative properties and column opacity. One would have to drive the model with a tuned opacity to reach an agreement with the observations, thereby losing its self-consistency. In this paper, we show that using the most recent dust radiative properties in the LMD (Laboratoire de Météorologie Dynamique) GCM solves this problem, which was mainly due to the underestimation of the dust single scattering albedo in the solar domain. However, significant temperature biases remain, especially above the 1 hPa pressure level. We therefore refine the model by implementing a “semi-interactive” dust transport scheme which is coupled to the radiative transfer calculations. The right prediction of the dust layer depth allowed by this scheme then removes the last significant temperature biases. The LMD/GCM is now able to predict good temperatures without any tuning of the dust opacity used to guide the model. Remaining discrepancies are discussed, and could be the result of uncertainties in the dust particle sizes on the one hand, and the neglect of the radiative effect of water-ice clouds on the other.

3.3 Introduction

About 40 years ago, [Gierasch and Goody \(1972\)](#) demonstrated that the thermal structure of the Martian atmosphere cannot be accounted for by a single CO₂ atmosphere, without the contribution of atmospheric dust. Dust is, indeed, the main driver of the martian climate, and its radiative properties (extinction efficiency Q_{ext} , single scattering albedo ω_0 and asymmetry parameter g) have to be known in details to accurately predict the heating rates and temperatures in a Mars Global Climate Model (GCM).

The best way to simulate the details of the present climate is to drive the GCM with

observation-derived dust opacities. However, it has been difficult in the past to obtain realistic temperatures by using the exact observed dust opacity. The latter had to be tuned to reach reasonable temperatures, raising some doubts on either GCMs or dust radiative properties used to compute the heating rates.

The dust radiative properties are difficult to retrieve, and are associated with many uncertainties to which GCMs are extremely sensitive. For example, an uncertainty of 5% for a single scattering albedo ω_0 of about 0.9 in the solar domain corresponds to an error on the heating rate of about 50% (Forget et al., 1999). Thanks to the numerous new missions of the last decade, many improvements have been made in our knowledge of dust radiative properties, ultimately leading to the retrieval of the fundamental refractive index, both in the visible and infrared regions (Wolff et al., 2006, 2009). This allows to compute the single scattering parameters for dust particles of different sizes, which is essential to fully account for their effect on GCM temperatures. The goal of this paper is to find the best way to use this new dataset, in order to create a self-consistent climate model, i.e. a model in which temperatures and dust opacities are both consistent with observations.

For this, the following questions will be addressed :

- What are the effects of the new dust radiative properties on the LMD/GCM ?
- What is the impact of the dust layer properties (thickness and particle sizes) on the simulated temperatures ?
- What can we learn from radiatively active dust experiments about the spatial distribution and size of the dust particles ?

Three simulations will be carried out, and the corresponding model configurations are described in section 3.4. Temperatures predicted by the LMD/GCM when using the dust radiative properties of Ockert-Bell et al. (1997) and Forget (1998) on the one hand, and the more recent optical indices of Wolff et al. (2006, 2009) on the other, are analyzed in section 3.5 and compared to the TES temperature measurements (Smith, 2004). These two simulations are later referred to as case 1 and case 2 simulations. The GCM radiative scheme is then connected to a dust transport model, which computes the dust spatial distribution and particle size. The predicted spatial distribution is used to compute the 3D opacity field, and each opacity profile is then multiplied by a constant to match the dust column opacity observed by TES (Smith, 2004). The particle sizes are also used to compute spatially and temporally variable radiative properties. This simulation is referred to as case 3 simulation, and is analyzed in section 3.6. Both Martian years 25 and 26 are simulated, to evaluate the model under the clear conditions of MY26, and the dusty conditions of MY25, during which the 2001 global dust storm occurred. The radiative effect of water-ice clouds is not included in the model to focus on dust alone, and will be the subject of another article in the near future.

3.4 Modeling approach

Point sur..... 31
Les propriétés
radiatives de la
poussière

The three simulations described in this paper are summarized in Table 3.1. They have a resolution of $5.625 \times 3.75^\circ$ in the horizontal, and 25 levels in the vertical, from the ground to ~ 100 km. The two first simulations use a modified Conrath profile to describe the vertical distribution of dust (as was the case in Forget et al. (1999)), and constant

radiative properties. The last simulation uses interactive dust profiles and varying radiative properties, based on a dust transport model which predicts the shape of the dust vertical profile and the size of the dust particles. Each of the three simulations is further described below.

3.4.1 “Ockert-Bell et al.” model (case 1 simulation)

The dust layer is characterized by the amount and spatial distribution of dust, as well as the radiative properties of the dust particles. The amount of dust in the atmosphere is indirectly given by its dust optical depth ^{*} :

Voir la partie 2.5 pour plus de détails.

$$d\tau_\lambda = \frac{3}{4} \frac{Q_{\text{ext}\lambda} q}{\rho_p r_{\text{eff}} g} dp, \quad (3.1)$$

where Q_{ext} is the dust extinction efficiency, q the mass mixing ratio, ρ_p the dust particle density (2500 kg m^{-3}), and r_{eff} the effective radius. In case 1 and case 2 simulations, we assume an homogeneous size and extinction efficiency of the dust particles. Consequently, the opacity in each layer is directly proportional to the amount of dust q and the pressure differential dp . Since dust is not carried explicitly by the model in these simulations, a modified Conrath vertical profile is assumed (Conrath, 1975; Forget et al., 1999), and the dust opacity differential obeys the relation :

$$d\tau_\lambda(p) \propto dp \exp \left\{ 0.007 \left[1 - \left(\frac{p_{\text{ref}}}{p} \right)^{70/z_{\text{max}}} \right] \right\}, \quad (3.2)$$

where $p < p_{\text{ref}}$, with p_{ref} the reference pressure (6.1 hPa). When the atmospheric pressure p is larger than p_{ref} , the dust opacity is assumed constant. The dust layer top altitude parameter z_{max} is given by an analytical function that fits the measurements of z_{max} achieved by Jaquin et al. (1986) (see section 2.1 of Montmessin et al. (2004) for further information). The variation of this function at the equator is represented in Fig. 3.8.c (black sinusoid). The variations in z_{max} are identical from one martian year to another, and cannot capture the interannual variability of the dust layer thickness. The opacity profile 3.2 is then linearly scaled so that the dust column opacity in the model matches the observed TES opacity at $9.3 \mu\text{m}$ (see Fig. 3.8.b and Smith (2004)). It is worth reminding that TES opacity is an absorption opacity, and it has to be converted to an extinction opacity, which is the opacity actually needed by the GCM. As discussed in details by Wolff and Clancy (2003) (see section 7.2.1 therein), this conversion can be done without large error using a factor of 1.3. Consequently, $\tau_{\text{GCM}}(9.3 \mu\text{m}) = \tau_{\text{TES}}(9.3 \mu\text{m}) \times 1.3$, and the GCM is constrained by the observed and untuned dust opacity. This is true for all the simulations presented in this paper.

Once the opacity in each layer is known, the model needs the dust single scattering parameters, which will be used by the radiative transfer scheme. The radiative transfer codes at solar wavelengths and outside the $15 \mu\text{m}$ CO_2 band are both based on the two streams algorithm of Toon et al. (1989). Their channels include two solar bands ($0.1\text{-}0.5 \mu\text{m}$ and $0.5\text{-}5 \mu\text{m}$), the silicate band ($5\text{-}11.5 \mu\text{m}$), and the rest of the IR domain ($20\text{-}200 \mu\text{m}$). The net exchange formulation (Dufresne et al., 2005) is used in the $15 \mu\text{m}$ CO_2 band ($11.5\text{-}20 \mu\text{m}$), where dust scattering is neglected. In this band, only absorption by

Sim.	Dust single scattering properties		Opacity profiles*
	Dataset	Computation method	
# 1	Single scattering parameters of Ockert-Bell et al. (1997) and Forget (1998)	Spatially constant Direct merging of the two datasets using $T_{0.67\mu m}/T_{9\mu m} = 2$	Analytical function Modified Conrath profile
# 2	Refractive index $m = n + ik$ of Wolff et al. (2006, 2009)	Spatially constant T-Matrix generated using m Gamma dist. **, $r_{\text{eff}}=1.5 \mu m$, $v_{\text{eff}}=0.3$	Analytical function Modified Conrath profile
# 3	Refractive index $m = n + ik$ of Wolff et al. (2006, 2009)	Space-varying properties based on predicted sizes Log-normal dist. **, variable r_{eff} , $v_{\text{eff}}=0.3$	Model predicted Two-moment scheme

* Opacity profiles are always linearly scaled to match the column dust opacity measured by TES.
** Randomly oriented oblate cylinder with an axial ratio of 1.

TAB. 3.1 – Main characteristics of the three GCM experiments.

dust is taken into account, and added to that of CO₂ by using $Q_{\text{abs}} = Q_{\text{ext}} (1 - \omega_0)$ (Forget et al., 1999).

Providing dust radiative properties covering the entire solar and thermal infrared spectral range for climate modeling required long-term efforts. Several datasets have been available since Mariner 9 in 1972. The first general circulation models including a comprehensive radiative transfer model (Pollack et al., 1990; Haberle et al., 1993, 1997, 1999; Hourdin et al., 1993, 1995; Wilson and Hamilton, 1996) used solar spectrum averaged single scattering properties derived from Viking lander studies by Pollack et al. (1979) at solar wavelength and from Mariner 9 IRIS observations by Toon et al. (1977). This dust was relatively “dark” (solar averaged single-scattering albedo and asymmetry parameter were 0.86 and 0.79, respectively) and yielded warm atmospheric temperatures.

After the late 1990s, and until now, a second generation of models (Forget et al., 1999; Hartogh et al., 2005; Takahashi et al., 2006) benefited from the improved dataset achieved by Ockert-Bell et al. (1997) in the solar range, and Forget (1998) in the infrared range. It is this dataset which is used in case 1 simulation, and referred to as the “Ockert-Bell et al.” dataset. Later measurements by Clancy and Lee (1991) have been used in GCMs as well (Forget et al., 1999; Richardson et al., 2002), but with caution due to the unusually low value of the asymmetry factor g .

Ockert-Bell et al. (1997) extended Viking Lander data corrected by Pollack et al. (1995) to all solar wavelengths (0.2 - 4.2 μm), by using different spectra of bright surfaces under low dust conditions, acquired by the Orbiting Astronomical Observatory in the UV (Wallace et al., 1972) and by Phobos-2 ISM and earth-based telescopes in the visible and near-infrared range (Mustard and Bell, 1994). The infrared dataset (5-50 μm) was built on the work by Toon et al. (1977), who fitted IRIS/Mariner 9 spectra by using a sample of clay called Montmorillonite 219b. This dataset was adapted for GCMs by Forget (1998), who removed the 20 μm absorptions of this mineral which are not observed on Mars.

These first properties thus merge information from different instruments looking at different locations and times in the solar and thermal domains. Consequently, the dust particle size distributions (which control the balance between dust absorption at solar wavelengths and emission in the infrared region) are different from one observation to another, and thus different for the two domains. Consequently, the ratio of the extinction efficiency (and thus opacity) in the visible to the one in the infrared (later called the “solar over infrared ratio”) is specified to correct for this bias and merge both datasets.

Here, we use $\tau_{\text{GCM}}(0.67 \mu\text{m}) / \tau_{\text{GCM}}(9.3 \mu\text{m}) = 2$ (Forget, 1998; Toigo and Richardson, 2000). The resulting dust radiative properties are assumed constant in space and time.

3.4.2 “Wolff et al.” model (case 2 simulation)

The second unified dataset comes from MGS (Mars Global Surveyor) and MRO (Mars Reconnaissance Orbiter) overflights of the MERs (Martian Exploration Rovers), which enabled the simultaneous observation of dust both from the surface and from space by instruments having similar spectral windows.

Wolff et al. (2006, 2009) combined the “best parts” of each dataset in order to effectively isolate the average scattering properties of the suspended dust particles. More specifically, using the total column optical depth and surface reflectance properties from

MER with the multiangle, multispectral MGS (TES) and MRO (CRISM) observations, they constructed a self-consistent retrieval algorithm which returned the single scattering albedo and associated refractive indices. At the same time, the combined analyses minimized the typical model uncertainties generally encountered in atmospheric remote sensing analyses, i.e., surface reflectance/emission properties, consistent aerosol scattering with respect to wavelength and particle size, etc. Ultimately, the MER-MGS analyses constrain the 7.5-30 μm region while that for MER-MRO cover 0.26-3 μm . Wolff et al. (2009) extend this latter coverage to 4 μm through the MEX-OMEGA observations of Määttänen et al. (2009) * .

Paragraphe écrit par
Mike Wolff.

The resulting single scattering parameters are given in Fig. 3.4 (black line), where they are compared to the “Ockert-Bell et al.” properties (grey line). The “Wolff et al.” properties correspond to a Gamma size distribution of effective radius $r_{\text{eff}} = 1.5 \mu\text{m}$ and variance $v_{\text{eff}} = 0.3$. The dust particles are assumed to be cylindrical with an axial ratio of 1 (Wolff et al., 2001).

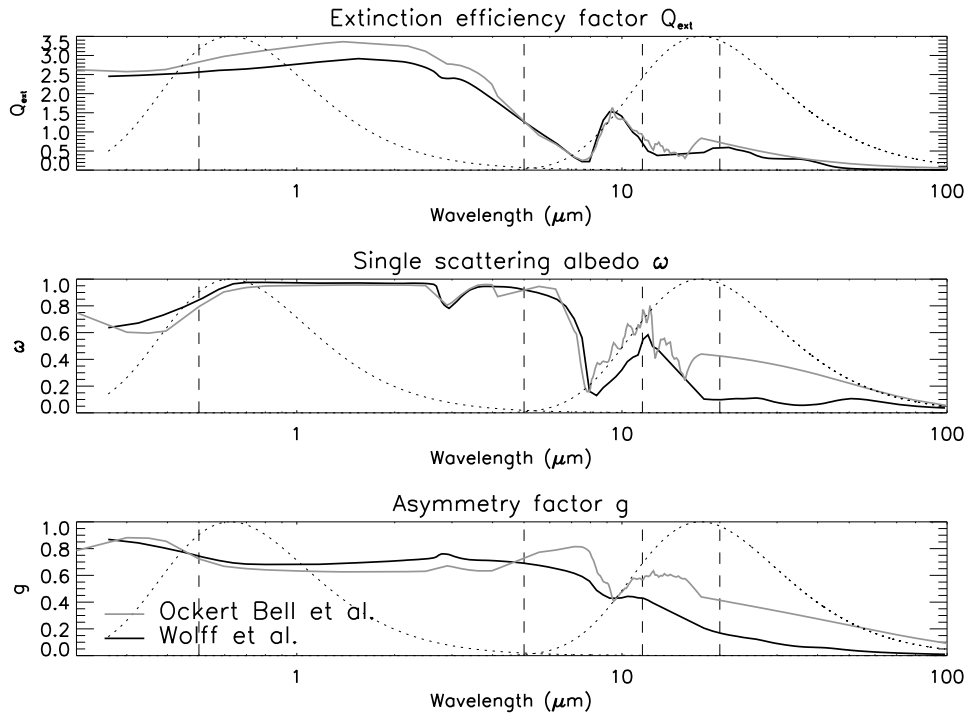


FIG. 3.4 – Dust single scattering parameters deduced by Ockert-Bell et al. (1997); Forget (1998) (grey line) and Wolff et al. (2006) (black line). From top to bottom : extinction efficiency factor Q_{ext} , single scattering albedo ω_0 and asymmetry parameter g . Dashed curves in the background represent the normalized blackbody emission spectra for temperatures of 5870K and 210K, respectively (area preserving representation). Vertical lines separate the 6 channels of the GCM radiative transfer scheme. X-axis is wavelength in micrometers.

Similarly to case 1 simulation, case 2 simulation is driven by the untuned TES dust opacity, and the radiative properties are assumed constant. The dust distribution again

follows a modified Conrath profile, and the dust layer top altitude is still given by an analytical function.

3.4.3 TES-normalized interactive dust model (case 3 simulation)

The last simulation is designed to realistically simulate the vertical distribution and size of the dust particles. This allows us to compute the true opacity in each layer (equation 3.1) and to take into account the size of the dust particles in the calculation of the single scattering parameters.

Dust transport scheme

An efficient way to predict the evolution of dust particles is to use a so-called two-moment scheme, used for example by Schulz et al. (1998) to model Saharan dust plumes. If we assume that in any atmospheric layer the size of the dust particles can be described by a lognormal distribution, then three parameters are sufficient to describe the dynamics of the whole particle population. Indeed, the number of particles in each size bin is given in this case by :

$$n(r) = \frac{N}{\sqrt{2\pi} \sigma_0 r} \exp \left[-\frac{1}{2} \left(\frac{\ln(r/r_0)}{\sigma_0} \right)^2 \right], \quad (3.3)$$

where $n(r) dr$ is the number of dust particles per kg in the size range $[r, r + dr]$, N the total number of particles per kg, and r_0 and σ_0 the mean and standard deviation of the distribution. The moments of the lognormal distribution are conveniently expressed by :

$$M_k = \int_0^\infty r^k n(r) dr = N r_0^k \exp \left(\frac{k^2}{2} \sigma_0^2 \right). \quad (3.4)$$

Consequently, the lognormal distribution is entirely described by N , r_0 and σ_0 . Furthermore, the mass mixing ratio q is directly related to r_0 by :

$$\begin{aligned} q &= \int_0^\infty \frac{4}{3} \pi r^3 \rho_p n(r) dr \\ &= \frac{4}{3} \pi \rho_p M_3 \\ &= \frac{4}{3} \pi \rho_p N r_0^3 \exp \left(\frac{9}{2} \sigma_0^2 \right). \end{aligned} \quad (3.5)$$

Therefore, if we assume that the standard deviation σ_0 is constant, the distribution is fully described by the number of particles per kg N and the mass mixing ratio q . The evolution of the dust size distribution can thus be predicted by the GCM using only two tracers. This method is often called a two-moment scheme because N is equal to M_0 and q is directly related to M_3 . The effective radius of the dust population is then expressed as :

$$r_{\text{eff}} = \left(\frac{3}{4} \frac{q}{\pi \rho_p N} \right)^{1/3} (1 + v_{\text{eff}}). \quad (3.6)$$

32 Point sur
Le modèle de transport à deux moments

Consequently, dust is represented in the GCM by two tracers, which are injected in the atmosphere by specifying two spatially constant lifting rates $\partial_t q$ and $\partial_t N$. As reported by [Kahre et al. \(2008\)](#), a spatially and temporally constant lifting rate is sufficient to predict, at least to first order, the spatial distribution of dust particle sizes. The two tracers are advected by a Van Leer scheme I ([van Leer, 1977](#); [Hourdin and Armengaud, 1999](#)). Sedimentation depends on the size of the particles, and the lognormal distribution is discretized into 12 size bins where the sedimentation flux of each tracer is computed. The shape of the particles is accounted for by using the additional β factor in the second term of the Cunningham correction factor (see [Murphy et al., 1990](#)). Best results are obtained by setting β to 0.5, as reported by [Murphy et al. \(1990\)](#) when simulating the decay of the 1977A planet-encircling dust storm. The effective radius and variance of the lifted population are set to $3 \mu\text{m}$ and 0.5 respectively, so that the predicted r_{eff} in the lower levels of the GCM matches the observations of [Wolff et al. \(2006\)](#) (see Fig. 20 and 21 therein).

Online single scattering parameter calculation

The dust particle sizes predicted by the two-moment scheme (see equation 3.6) are used to compute, in the GCM, a single scattering parameter field that evolves in space and time. We therefore account for the change in scattering through the dust layer created by differential sedimentation of the dust particles.

To do so, the single scattering parameters for a set of dust particle sizes are computed offline and stored in a look-up table which is loaded by the GCM at the beginning of the simulation. This look-up table contains the single scattering parameters Q_{ext} , ω_0 and g for 50 populations of dust particles, which follow a lognormal distribution of small effective variance ($v_{\text{eff}} = 0.05$). This small variance is used to remove the ripples created by the interferences in the scattered field (see for example [Hansen and Travis, 1974](#), page 551), which otherwise prevent the accurate integration, in the GCM, of the single scattering properties, because of the relatively small number of particle sizes stored in the look-up table. The single scattering parameters are computed from the dust refractive index derived by [Wolff et al. \(2006, 2009\)](#) using the T-Matrix code of [Mishchenko et al. \(1996\)](#), and assuming cylindrical dust particles ($D/L=1$) ([Wolff et al., 2001](#)).

Then, the GCM uses this look-up table and the effective radius predicted by the dust transport scheme to compute in each grid box the integrated single scattering parameters. A 20-point Gauss-Legendre integration is employed, along with an interpolation grid that optimizes the computation time. A lognormal size distribution of effective variance $v_{\text{eff}} = 0.3$ is chosen, instead of the Gamma distribution used in case 2 simulation.

Scaling to the measured TES opacity

After calculating the dust sizes, single scattering properties and spatial distribution, the 3D opacity field can be accurately deduced. To do so, the predicted dust mass mixing ratio q (see equation 3.5), effective radius r_{eff} (see equation 3.6) and extinction efficiency factor $Q_{\text{ext}\lambda}$ (which depends on r_{eff}) are used to compute the opacity in each layer $d\tau_\lambda$ following equation 3.1. Then, each opacity profile is multiplied by a constant so that the dust column opacity matches the TES observations ([Smith, 2004](#)). Consequently, the dust transport model is “semi-interactive”, because it explicitly predicts the dust spatial

3.5. Results using a prescribed dust vertical distribution

distribution, but uses observations to scale each opacity profile employed in the radiative transfer calculations.

The resulting density-scaled opacity at $0.67 \mu\text{m}$ is represented in figure 3.5, along with the effective radius r_{eff} in contours (micrometers). The fields are averaged zonally and over the $L_s = 210\text{-}240^\circ$ period for MY25 (left) and 26 (right). The density-scaled opacity follows from equation 3.1 and the hydrostatic equilibrium, and can be written as :

$$-\frac{1}{\rho_a} \frac{d\tau_\lambda}{dz} = g \frac{d\tau_\lambda}{dp} = \frac{3}{4} \frac{Q_{\text{ext}\lambda} q}{\rho_p r_{\text{eff}}}, \quad (3.7)$$

where ρ_a is the atmospheric density in kg m^{-3} . The 2001 global dust storm is clearly visible in the left panel, where dust particles of $1.6 \mu\text{m}$ in size are found near the equator, at an altitude of around 20 km. The density-scaled opacity reflects the dynamics of the solstitial Hadley cell, with dust-raising and transport occurring over the southern mid-latitudes.

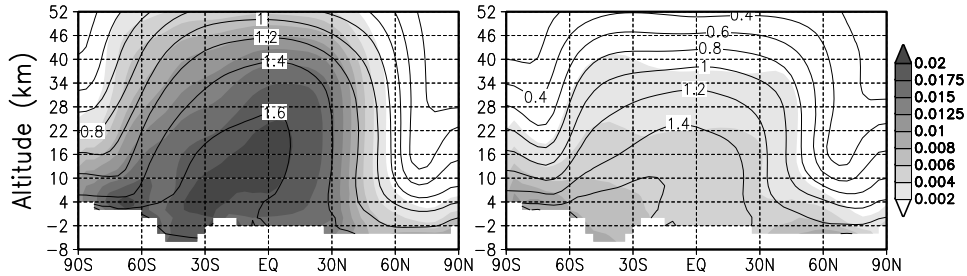


FIG. 3.5 – Density scaled opacity $g d\tau/dp$ (shaded colors) at $0.67 \mu\text{m}$ and dust effective radius r_{eff} (contours, in μm) averaged zonally and over the $L_s = 210\text{-}240^\circ$ period for MY25 (left) and MY26 (right). Altitude is given in km above areoid.

Dust particle sizes are larger for MY25 than for MY26 because the TES opacity increases, warms the GCM atmosphere, and feeds back on the Hadley cell intensity. Consequently, the “semi-interactive” method allows us to capture the main characteristics of the dust layer, without losing control of its total opacity.

3.5 Results using a prescribed dust vertical distribution

In this section, we analyze the temperature biases found in the GCM simulations when the dust distribution is prescribed and the radiative properties are spatially and temporally constant (case 1 and 2 simulations). The analysis will be based on Fig. 3.6, 3.7 and 3.8.

Figures 3.6 and 3.7 illustrate the zonal and diurnal mean temperature difference between the GCM simulations and the TES measurements ($\Delta T = T_{\text{GCM}} - T_{\text{TES}}$) for MY25 and 26, respectively. The results are averaged over 30° of L_s periods. A positive ΔT reflects a warm bias in the GCM simulation. We only focus on the $\pm 50^\circ$ latitude band, because the temperature biases in the polar regions are hard to interpret without accounting for the radiative effects of water ice clouds. Four seasons are represented : one near the aphelion, and three during the dusty perihelion period. The TES diurnal mean temperatures

to which the GCM temperatures are compared are given for reference on the left side of the figure. Figure 3.8 provides the 2 PM equatorial temperature at the 0.5 hPa level (panel a), along with the dust opacity at $9.3 \mu\text{m}$ observed by TES (panel b), the dust layer top altitude (panel c), the effective radius of the dust particles at the 0.5 hPa pressure level (panel d), and the water-ice cloud opacity at $12.1 \mu\text{m}$ measured by TES (panel e).

The differences in temperature seen in these figures can come from unresolved dynamical and physical processes, as well as errors in the prediction of the distribution and radiative effect of aerosols.

3.5.1 “Ockert-Bell et al.” model

The first simulation uses the dust radiative properties derived by Ockert-Bell et al. (1997) and adapted for the GCM by Forget (1998). It is worth reminding that these radiative properties are spatially and temporally constant. The temperature differences between this first GCM simulation and the TES dataset for MY25 and 26 are summarized in the second column of Figure 3.6 and 3.7. During the cloud season (second panel on the first line of Fig. 3.6 and 3.7), there is a cold bias in the GCM located above the 0.5 hPa level. It is now well established that this cold bias results from the absence of radiatively active clouds in the GCM (Wilson et al., 2007; Wilson et al., 2008). Apart from the cold bias due to water-ice clouds, the GCM overestimates temperature by about 10 K, especially during the perihelion season (see the three last lines in Fig. 3.6 and 3.7). This is also clearly seen in Fig. 3.8.a, where the temperature at the 0.5 hPa level of the case 1 simulation (blue line) is always greater than the observed TES temperature (black crosses). The only exception is the cloud season (see Fig. 3.8.a around $L_s = 90^\circ$), where the cold bias resulting from the absence of radiatively active clouds in the GCM is compensated by the overall warm bias.

As we mentioned in the introduction, our knowledge of dust radiative properties has increased in the last decades, and it became apparent that the dust single scattering albedo $\omega_0 = 0.89$ (solar irradiance-weighted average) retrieved by Ockert-Bell et al. (1997) was lower than the values found by Clancy and Lee (1991); Clancy et al. (2003) and more recently by Vincendon et al. (2007); Määttä et al. (2009); Wolff et al. (2009), which are nearly equal to 0.94. Consequently, it has been expected that the low value of ω_0 will result in overestimated temperatures in climate models (Wolff et al., 2009). This would explain why there is a general warm bias in case 1 simulation. In the next section, the radiative properties of dust are updated to test this hypothesis.

3.5.2 Effect of the new “Wolff et al.” radiative properties

The radiative properties are now updated to the most recent dataset derived by Wolff et al. (2009), and the resulting single scattering parameters are shown in Fig. 3.4. The main difference between the “Ockert-Bell et al.” (grey line) and the “Wolff et al.” (black line) properties lies near the peak of the solar emission spectrum, where the single scattering albedo retrieved by Wolff et al. (2009) is higher than the one measured by Ockert-Bell et al. (1997). It means that the absorption by dust was probably overestimated in case 1 simulation. The two ω_0 at $0.67 \mu\text{m}$ differ by about 4% (0.970 for case 2 and 0.929 for case 1

3.5. Results using a prescribed dust vertical distribution

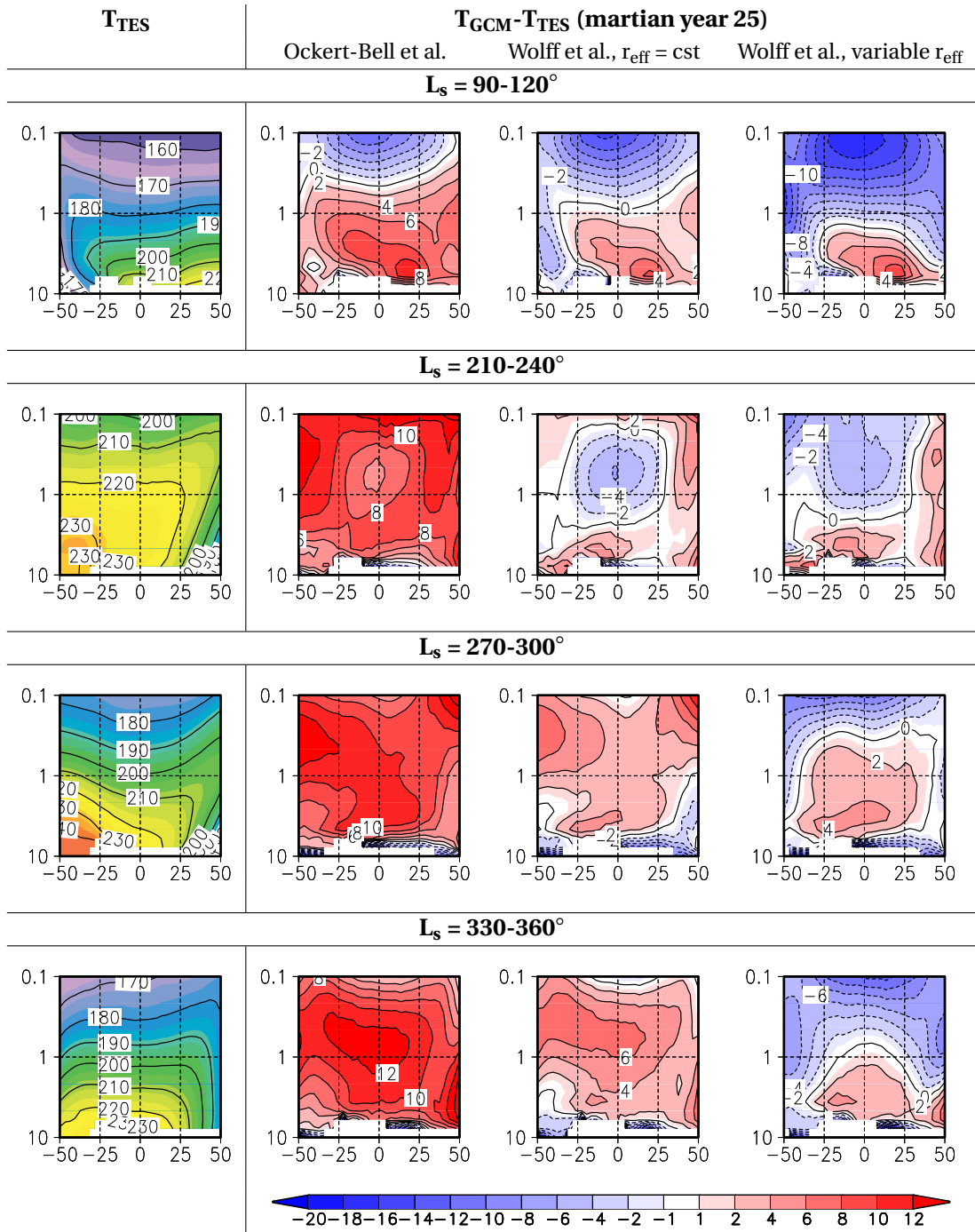


FIG. 3.6 – **1st column** : Zonally and time averaged (over 30° of L_s) temperature fields as measured by TES (Smith, 2002) for martian year 25. Contour interval is 10 K. **2nd, 3rd and 4th column** : Temperature difference between the LMD/GCM and TES averaged over the same time period and for the three reference simulations described in section 3.4. Contour interval is 2 K. Y-axis is pressure in hPa.

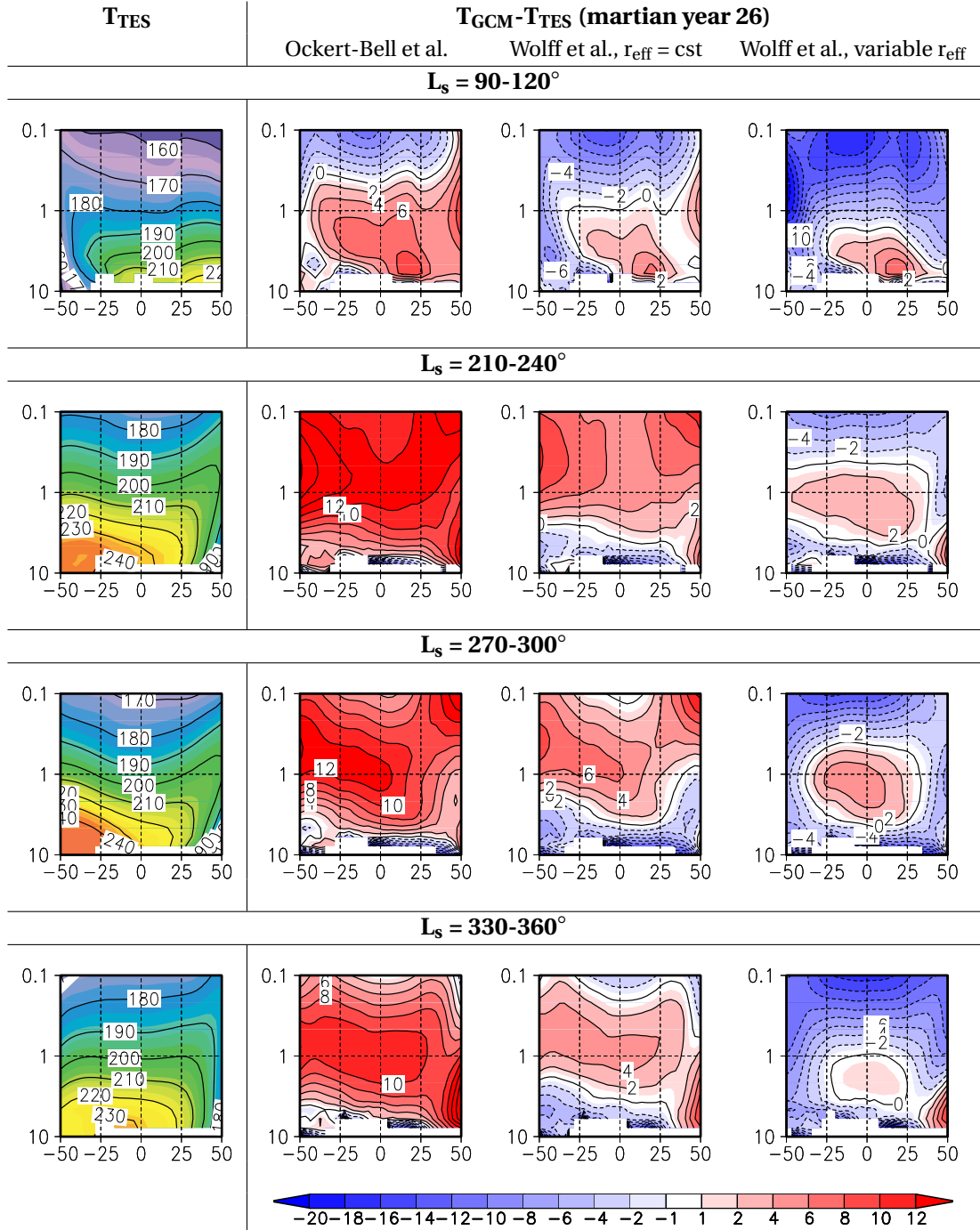


FIG. 3.7 – Same as Fig. 3.6 but for martian year 26.

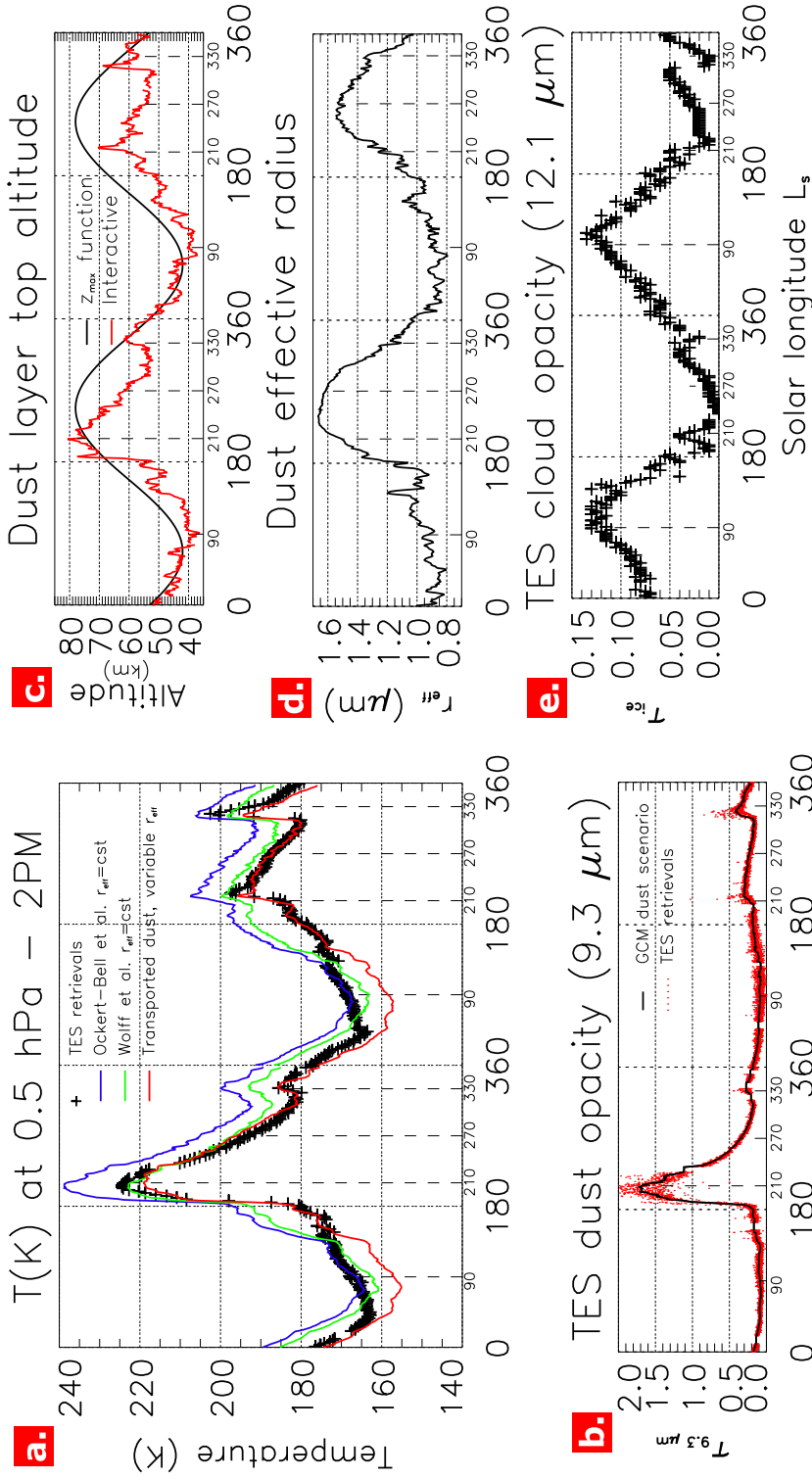


FIG. 3.8 – (a) Zonally averaged equatorial temperature at 2 PM for the 0.5 hPa pressure level from TES climatology (crosses, Smith, 2004, martian year 25 and 26), and as predicted by the LMD/GCM for three different cases : a simulation using the Ockert-Bell radiative properties (blue curve), another simulation using the Wolff et al. properties (green curve) and a last simulation that uses a semi-interactive dust model (red curve). Vertical dashed lines indicate the four different seasons that are further depicted in Fig. 3.6 and Fig. 3.7. (b) Dust opacity at $9.3 \mu\text{m}$ used to guide the model (in black), compared to the raw TES dataset at 2 PM (red points). (c) Analytical Z_{max} function used for simulation 1 and 2 (black line), compared to the dust layer top altitude actually predicted by the model in simulation 3 (red line). (d) Dust effective radius predicted by the GCM at the 0.5 hPa level for case 3 simulation. (e) Cloud opacity at $12.1 \mu\text{m}$ measured by TES (Smith, 2004). All the variables are zonally averaged and taken at the equator.

simulation), which corresponds to significant changes in the predicted heating rates, as mentioned in the introduction.

The expected cooling effect of the new dust properties is apparent during the dust season in Fig. 3.6 and 3.7 (lines 2 to 4, third column). The warm bias is reduced by 6-8 K, but the model still overestimates temperature, especially near the 1 hPa level. Consequently, using a brighter dust improves the results, but significant differences remain.

The periods of largest temperature anomalies can be identified in Fig. 3.8.a, where the temperature at the 0.5 hPa level is represented in green. The model fails in reproducing the temperature variability before and after the peak of the dust storm (right before $L_s = 180^\circ$ and at $L_s = 330^\circ$) for MY25, and at $L_s = 180^\circ$ for MY26, at seasons when the cloud opacity is relatively low (see Fig. 3.8.e). These differences cannot be attributed to the dust opacity scenario (see Fig. 3.8.b), which presents the same behaviour as the measured temperature. For example, before the peak of the 2001 dust storm, at $L_s = 180^\circ$, the observed rise in temperature is sudden, as is the case in the dust opacity scenario. Why does the GCM fail in reproducing these sudden temperature increases ?

These biases have also been reported by Wilson et al. (2008), who observed a temperature anomaly of 2 to 4 K for MY24 and 26, and a less pronounced bias for MY25. They attributed these departures from the observed temperatures to variations in the dust depth and particle sizes which were not represented in their control simulation, which is also our case. If this hypothesis is correct, we can expect case 3 simulation to return better results.

Finally, a cold bias of around 4 K is found near the 1 hPa level in the peak of the 2001 dust storm (see Fig. 3.6, line 2, third column). There are many possible explanations for this cold bias. The dust layer top altitude might be larger than the specified z_{\max} (see section 3.4.1), and the size of the dust particles, larger than the one used to compute the spatially constant dust radiative properties ($r_{\text{eff}} = 1.5 \mu\text{m}$). Dust transport experiments performed by Kahre et al. (2008) have also revealed the formation of an enriched dust layer during storm periods at an altitude that corresponds to our cold bias. The modified Conrath profile (see equation 3.2) is in this case not well suited to reproduce this local maximum in dust content.

These results motivated the development of case 3 simulation, where the dust vertical distribution and particle size are predicted by the model and taken into account in the radiative calculations. The results of this simulation are analyzed in the next section.

3.6 Results of the semi-interactive dust model

3.6.1 Role of the dust depth and particle size

In this last simulation, the dust spatial distribution and radiative properties are varying based on the predictions of the semi-interactive dust model. The results are presented in the last columns of Fig. 3.6 and 3.7. Below 1 hPa, the temperatures predicted by case 2 and case 3 simulations are similar. Indeed, the size distribution of the lifted population is chosen so that the effective radius of the particles in the lower atmosphere is consistent with the measurements of Wolff et al. (2006). We use the same dust refractive index, and the dust layer is often well represented by a modified Conrath profile at these

altitudes. Consequently, we can expect the two simulations to give similar results in the lower atmosphere.

However, a general cooling is observed near and above the 1 hPa pressure level. During the aphelion season ($L_s = 90-120^\circ$, first line of Fig. 3.6 and 3.7), the cold bias due to the absence of radiatively active clouds in the model is more pronounced. During the perihelion season, the warm biases that were present in case 2 simulation almost disappear. Near the 1 hPa pressure level, the warm bias is acceptable and reduced to ~ 2 K. The details of the temperature variations at the 0.5 hPa level are represented in Fig. 3.8.a. A much better agreement is seen between the model temperature and the observations, and the only discrepancy occurs during the aphelion season, when the cloud opacity at $12.1 \mu\text{m}$ is higher than ~ 0.07 (see panel e of Fig. 3.8). This temperature difference during the aphelion season is expected, because the radiative effect of clouds is neglected in our simulations. Since the rest of the model temperature curve fits the observation, an assessment of the radiative heating of clouds can be made, and is found to reach 10 K.

As described in section 3.5.2, case 2 simulation tends to overestimate temperature, especially before and after the global dust storm of MY25, and near $L_s = 180^\circ$ for MY26 (panel a of Fig. 3.8, green curve). In case 3 simulation, these departures from the observations are corrected (see the red curve in Fig. 3.8.a). The sudden rise in temperature before the global dust storm of MY25, as well as the decrease in temperature during the decay of the storm, are well reproduced. Similarly, the model temperature now follows the observations near $L_s = 180^\circ$ for MY26. These improvements are mainly due to the better assessment of the dust layer top altitude, which is illustrated in panel c of Fig. 3.8 (red line), and compared to the z_{max} parameter used in case 1 and 2 simulations (black line). It is seen that the previously prescribed z_{max} can be larger than the simulated dust depth by as much as 20 km, especially when warm biases were observed. The same can be said of the simulated size of the dust particles (panel d of Fig. 3.8), which is most of the time lower than the values used to compute the spatially constant single scattering parameters of case 1 and 2 simulations.

Consequently, the model was overestimating the amount and size of the dust particles at high altitudes in case 1 and 2 simulations, thereby absorbing too much solar radiation and overestimating the heating rates. This result is consistent with the early expectations of Wilson et al. (2008), and with the preliminary radiative experiments performed by Kahre et al. (2008) (see section 6.5 therein). Supplementary simulations show that the temperature improvements in case 3 simulation are mostly due to the right assessment of the dust depth, rather than to the changes in radiative properties due to dust particle sizes. Indeed, if the size of the dust particles is kept constant at a value of $1.5 \mu\text{m}$ for the radiative transfer calculations of case 3 simulation, the temperatures are only modified by about ± 1 K compared to the complete simulation. The impact of varying dust particle sizes on the temperatures is thus secondary compared to that of dust vertical profile. It does not mean that the effect of dust particle size is negligible, as we will see in the next section.

3.6.2 Remaining temperature biases

Despite the overall improvement provided by the semi-interactive dust model, a cold bias is seen near the 0.1 hPa pressure level, even outside the cloud season (last column of Fig. 3.6 and 3.7). This cold bias is less pronounced during the peak of the 2001 global dust storm (last column and second row of Fig. 3.6), where it is close to -4 K. It is also relatively weak during MY26 for the $L_s = 210\text{-}240^\circ$ period. Interestingly, these two periods correspond to the lowest cloud opacities (see Fig. 3.8.e). The rest of the perihelion season is characterized by a cold bias that can exceed -10 K. Such bias has also been noticed in simulations performed by Basu et al. (2004), using the GFDL Mars GCM.

We see two possible explanations for this cold bias. The first one is an underestimation of the amount of dust at these altitudes. This would suggest that the dynamics of the dust layer is not well captured by the unimodal size distribution employed in our dust transport scheme. A bimodal size distribution of martian dust particles has been suggested in the past, for example by Montmessin et al. (2002), who proposed the existence of a population of submicron particles to explain an observation of the Viking Orbiter camera. Another population of submicron particles would reach higher altitudes in the model, and warm the layers where a cold bias is present. The second hypothesis is the presence of fine water-ice clouds. Indeed, the cold bias, as we mentioned, seems to vary as a function of cloud opacity. For example, the cold bias is weaker for the $L_s = 210\text{-}240^\circ$ period of MY26 than for the $L_s = 330\text{-}360^\circ$ period, during which the aphelion cloud belt starts to form (see the second and fourth line in Fig. 3.7). Consequently, analyzing the radiative effect of water-ice clouds is the next necessary step to better understand the origin of this cold bias.

Interestingly, the cold bias observed during the 2001 dust storm near the 1 hPa level in case 2 simulation is unchanged, despite the prediction by the model of a high dust opacity layer at this altitude (see the left panel in Fig. 3.5). This suggests that it is not the dust vertical profile but rather the predicted particle size that is not well reproduced by the model under storm conditions.

Finally, a cold bias also occurs during rapid dust opacity increases. It can be seen in Fig. 3.8.a, during the peak of the 2001 dust storm ($L_s = 210^\circ$) and also during the two regional dust storm of MY26 ($L_s = 220^\circ$ and $L_s = 320^\circ$). During these short periods, TES temperature increases suddenly, and the GCM does not reproduce this behaviour. The dust transport model might fail in raising the right amount of dust at these altitudes, or, as mentioned above, the model might underestimate the size of the dust particles inside the storm. Another possibility is the underestimation of dust opacity during these storm events. As we can see in Fig. 3.8.b, there is a dispersal of the TES opacity values (red dots) during the three periods mentioned above. This variability is smoothed out in the dust opacity scenario of the GCM (black line), and this might also explain why the resulting temperatures are lower than observed.

3.7 Conclusion

It has been difficult in the last decade to predict, in the LMD/GCM, a realistic temperature while using at the same time the observed dust opacity values. Indeed, the model

tended to overestimate temperature if the dust opacity used to drive the model was not properly tuned. In this paper, we identify the origin of this disagreement by using the most recent dust radiative properties, and we refine our analysis in an attempt to be the closest to the observed TES temperatures. The main results can be summarized as follows :

- The use of the most recent dust radiative properties (Wolff et al., 2006, 2009) allows a good prediction of the atmospheric temperatures, while being at the same time consistent with the opacity values measured by TES. The temperature overestimation in previous versions of the GCM was the result of dust being too dark in the Ockert-Bell et al. (1997) dataset. Indeed, the dust single scattering albedo at $0.67 \mu\text{m}$ retrieved by Wolff et al. (2009) is higher by 4% than the value measured by Ockert-Bell et al. (1997) (see Fig. 3.4, second panel). As illustrated in Fig. 3.8.a, the 2 PM temperatures at the 0.5 hPa level are clearly overestimated when using the “Ockert-Bell et al.” radiative properties (blue line), whereas a good agreement is achieved by using the “Wolff et al.” properties (green line). However, significant warm biases remain near and above the 1 hPa level, especially before and after dust storm events.
- Using a dust transport scheme to account for the spatial distribution and size of the dust particles in radiative transfer calculations removes the above mentioned warm biases (red line in Fig. 3.8.a). We show that the dust layer top altitude prescribed in the previous versions of the model was often too high, resulting in too much absorption of solar radiation by dust in the middle atmosphere. This finding is consistent with the early expectations of Wilson et al. (2008), and underlines the importance of accurately assessing the dust layer depth in Mars climate models.
- In all simulations, a cold bias is persistent near the 0.1 hPa pressure level. The relatively warm temperatures seen in the TES dataset might be due to radiatively active water-ice clouds, and/or to a population of small dust particles present at high altitude. It would suggest the existence of a bimodal size distribution, instead of the unimodal size distribution assumed in our dust transport model. A cold bias is also noticed near the 1 hPa level during the peak of the 2001 dust storm, suggesting that the dust particle sizes are larger in reality than in the model.

Adding radiatively active water-ice clouds will clarify the origin of the remaining differences between the LMD/GCM and the TES temperatures, and will allow us to extend the present analysis to the polar regions. This work is currently underway and will be the subject of a future article.

Next steps include the building of new dust opacity scenarios, the modeling of recent martian years, and the study of the Mars Climate Sounder observations, which already revealed many fascinating processes (McCleese et al., 2008; Kleinböhl et al., 2009; Heavens et al., 2010).

